Fabrication of vulcanized cross-linked polystyrene grafted on carbon nanotubes for use as an advanced lithium host

KE Xian-lan[1], LU Yu-heng[1], WU Jin-lun[2,*], WU Ding-cai[1,*]

（1. *PCFM Lab*, *School of Chemistry*, *Sun Yat-sen University*, *Guangzhou* 510006, *China*;

2. *Guangdong Cardiovascular Institute*, *Guangdong Provincial People's Hospital*, *Guangdong Academy of Medical Sciences*, *Guangzhou* 510080, *China*）

Abstract: We report the fabrication of vulcanized cross-linked polystyrene grafted on carbon nanotubes (CNTs) for use as an advanced three-dimensional Li host. First, polystyrene was grafted from Br-modified CNTs to form brush-like structure by surface-initiated atom-transfer radical polymerization. Polystyrene grafted on carbon nanotubes was then cross-linked using a Friedel-Crafts reaction and finally vulcanized with sulfur. Vulcanized cross-linked polystyrene grafted on carbon nanotubes was used as a support for the Li metal, and its macro-, meso- and microporous structure increased Li ion transport, buffered the volume changes of the Li anode, and provided a high specific surface area to reduce local current density, which assisted rapid and uniform Li plating/stripping. At the same time, the homogenously distributed sulfur in the support reacted with Li to produce a Li_2S-containing SEI layer, while the CNTs provided conductive pathways for the rapid transmission of electrons. As a result, a Li|Li symmetric cell using this anode material and a Cu current collector had a stable cycling performance of more than 500 h at a current density of 1 mA cm^{-2}. When $LiFePO_4$ was used as the cathode, a full cell had a high discharge capacity of 101 mAh g^{-1} with a capacity retention of 77% after 600 cycles at 1 C.

Key words: Vulcanized hypercrosslinked polystyrene brushes; Carbon nanotube substrates; Advanced lithium hosts; Li_2S-containing SEI; Lithium metal batteries

1 Introduction

The rapid development of wearable electronics, smart grid systems and electric vehicles has put forward increasing demand for high-energy-density electrochemical energy storage devices. Lithium (Li) metal is regarded as the most promising anode material toward next-generation batteries due to its highest theoretical specific capacity (3 860 mAh g^{-1}) and lowest redox potential (−3.04 V *vs*. standard hydrogen electrode)[1]. Nevertheless, the commercialization of Li metal batteries (LMBs) is seriously plagued by the growth of dendrites, the formation of fragile solid electrolyte interphases (SEI), and the serious volume fluctuation of Li metals[2–3]. Specifically, inhomogeneous Li deposition and continuous electrolyte consumption would cause erratic anode/electrolyte interface, leading to low coulombic efficiency and rapid capacity decay of LMBs[4–5]. What's worse, the volume fluctuation of Li anodes accompanied by the growth of dendrites could cause penetration of separators, giving rise to battery failure and even safety issues[4,6–7]. Therefore, the development of dendrite-free and interface-stable Li anodes is of great significance for the practical application of LMBs.

Three-dimensional (3D) nanostructured hosts have attracted increasing research interest to address these issues associated with Li anodes because of the largely reduced local current density and relieved volume fluctuation during Li plating/stripping[8–9]. Porous carbons are employed as ideal Li hosts due to their relatively chemical stability and high electronic conductivity, whereas the lithiophobic property could result in large Li deposition barriers[10–11]. Despite modification of 3D Li hosts with lithiophilic components is proved to homogenize Li ion flux and facilitate Li nucleation effectively[12–14], many lithiophilic components attached into these 3D Li hosts usually exist in the form of large particles. Recently, porous polymers with inherent lithiophilic properties (e.g.,

Received date: 2023-03-22; **Revised date:** 2023-05-29

Corresponding author: WU Jin-lun, Ph.D. E-mail: wujinlun@gdph.org.cn;
WU Ding-cai, Ph.D, Professor. E-mail: wudc@mail.sysu.edu.cn

Author introduction: KE Xian-lan, Master Student Candidate. E-mail: kexlan@mail2.sysu.edu.cn

Supplementary data associated with this article can be found in the online version.

poly-melamine-formaldehyde[15], polyaniline[16] and polypyrrole[17]) are used as fascinating hosts to ensure smooth and reversible Li plating/stripping. However, porous polymer hosts often possess poor ability to conduct electrons[9,11]. Furthermore, most of the 3D Li hosts mainly focus on retarding the growth of Li dendrites and alleviating the volume fluctuation of anodes, while the problem of unstable anode/electrolyte interface triggered by fragile SEI also requires sufficient attention[18]. Therefore, it is highly competitive yet remains a considerable challenge to simultaneously construct a high-lithiophilic host as well as robust SEI layer for dendrite-free and anode/electrolyte interface-stable LMB.

Herein, we have successfully developed a novel class of vulcanized cross-linked polystyrene grafted on carbon nanotubes (CNT-*g*-*sx*PS) which are utilized as advanced 3D Li hosts through the combination of surface-initiated atom transfer radical polymerization (SI-ATRP), Friedel-Crafts cross-linking chemistry and vulcanization reaction. As-obtained CNT-*g*-*sx*PS possess sulfur-abundant hierarchical porous nanonetworks, where macro/mesopores are derived from the interbrush cross-linking while abundant micropores come from the intrabrush cross-linking of polystyrene. On the one hand, the hierarchical macro-, meso- and microporous structure can accelerate Li ion transport, buffer volume fluctuation of the Li anode, and provide high specific surface area to reduce the local current density, which is beneficial for rapid and uniform Li plating/stripping. On the other hand, homogenously distributed sulfur groups in porous skeleton can react with Li to *in-situ* generate Li_2S-containing SEI layer, contributing to a stable anode/electrolyte interface (Fig. 1a). Moreover, carbon nanotube substrates act as rapid electron transmission pathways. As a result, the Li|Li symmetric cell with the CNT-*g*-*sx*PS@Cu/Li anode exhibits stable cycle performance of more than 500 h at 1 mA cm^{-2}. When paired with LFP cathode, the full cell with the CNT-*g*-

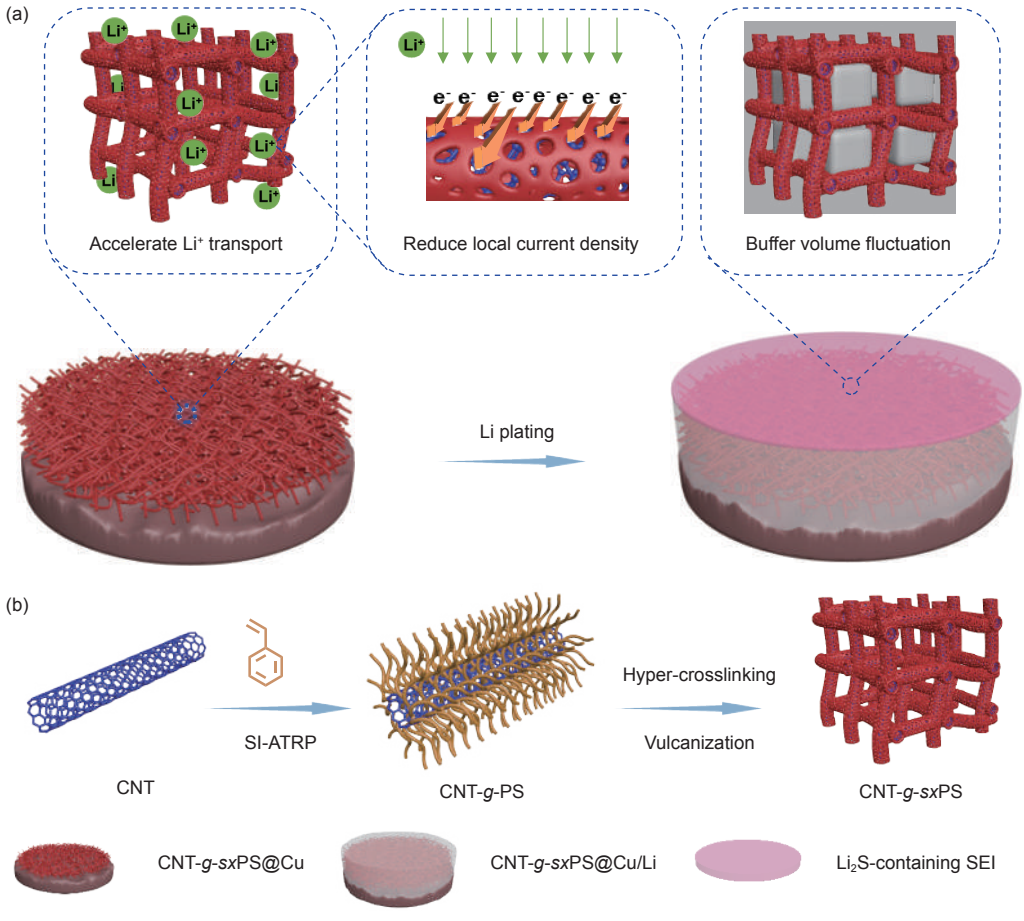

Fig. 1 (a) Schematic illustration of Li plating/stripping behavior on CNT-*g*-*sx*PS@Cu. (b) Synthetic route for the preparation of CNT-*g*-*sx*PS

*sx*PS@Cu/Li delivers a high discharge capacity of 101 mAh g^{-1} with a capacity retention of 77% after 600 cycles at 1 C.

2 Experimental

2.1 Materials

Styrene (Tianjin Yongda Chemical Reagent Co., LTD.) was purified by passing through a basic alumina column before use. Cuprous bromide (Aladdin, 99.99%), carbon nanotube (7011, Guangdong Canrd New Energy Technology), N, N-dimethylformamide (Aladdin, AR), thionyl chloride (Aladdin, AR), glycol (Aladdin, HPLC), trichloromethane (Aladdin, AR), 4-dimethylaminopyridine (Aladdin, AR), tetrahydrofuran (Aladdin, AR), triethylamine (Aladdin, AR), carbon tetrachloride (Macklin, AR), anhydrous aluminum chloride (Macklin, AR), elemental sulfur (Macklin, GR), carbon disulfide (Aladdin, AR) and others were used as received.

2.2 Preparation of CNT-*g*-*sx*PS

CNT-*g*-*x*PS were prepared according to previous literature[19]. CNT-*g*-*x*PS and elemental sulfur (1∶4) were thoroughly mixed and put into a porcelain boat wrapped with aluminum foil. After that, the mixture was annealed at 200 °C for 2 h and 280 °C for another 4 h under N_2 atmosphere. CNT-*g*-*sx*PS were collected after washing with carbon disulfide for 3 times, followed by vacuum drying at 40 °C overnight.

2.3 Preparation of CNT-*g*-*sx*PS@Cu

CNT-*g*-*sx*PS and polyvinylidene fluoride (9∶1) were dispersed into N-methyl-2-pyrrolidone, and the slurry was blade-coated onto one side of the commercial Cu foil. After vacuum drying at 70 °C overnight, CNT-*g*-*sx*PS@Cu were obtained by punching into disks with a diameter of 14 mm. The mass loading of the CNT-*g*-*sx*PS is 3.4 mg cm^{-2}.

2.4 Material characterization

Scanning electron microscopy (SEM, Hitachi S-4800) was used to characterize the morphologies and structures of the samples. Elemental mappings were investigated by Energy dispersive X-ray spectroscopy attached to SEM instrument. Thermogravimetric analysis (TGA) was conducted under N_2 atmosphere on a NETZSCH TG 209F1 Libra instrument (30-800 °C, 10 °C min^{-1}). The X-ray diffraction (XRD) patterns were measured by a D-MAX 2200 VPC diffractometer with Cu-*K*α radiation at a scanning rate of 10° min^{-1} from 10° to 80°. Fourier transform infrared (FTIR) spectra were recorded at room temperature on a Bruker Equinox 55. X-ray photoelectron spectroscopy (XPS) measurements were carried out on an ESCALAB Xi+ spectrometer (Thermo Fisher) using 250 W monochromatized Al *K*α radiation. N_2 adsorption-desorption isotherms were deterrmined by the Micromeritics ASAP 2020 analyzer at 77 K. The BET surface area (S_{BET}) was analyzed by the Brunauer-Emmett-Teller (BET) theory. The pore size distribution was obtained by performing analysis of the N_2 adsorption-desorption isotherms based on local isotherms generated using density functional theory (DFT).

2.5 Electrochemical test

All electrochemical measurements were conducted using CR2032-type coin cells. Li|Cu half-cells were assembled using CNT-*g*-*sx*PS@Cu (or bare Cu) and metallic Li (11 mm in diameter) as the working and counter electrodes, respectively. The electrolyte used for Li|Cu half-cells was 1.0 mol L^{-1} lithium bis(trifluoromethanesulfonyl)imide (LiTFSI) in a mixture of 1,3-dioxolane and 1,2-dimethoxyethane (1∶1 by volume) with 1% (mass fraction) $LiNO_3$ as additive. Before cycling test, Li|Cu half-cells were activated for 5 cycles between 0 and 1 V (*vs*. Li^+/Li) at 50 μA. Average coulombic efficiency was investigated in Li|Cu half-cells using standard Aurbach protocol[20]. In detail, CNT-*g*-*sx*PS@Cu was preconditioned with a single Li deposition/stripping cycle at 1 mA cm^{-2} and 10 mAh cm^{-2}. Subsequently, 10 mAh cm^{-2} Li was plated on CNT-*g*-*sx*PS@Cu at 1 mA cm^{-2}. Finally, 1 mAh cm^{-2} Li was stripped/plated repeatedly for 20 cycles at 1 mA cm^{-2}, followed by stripping out all Li until 1 V.

Li|Li symmetric cells were assembled using Li foils (11 mm in diameter) as the counter electrodes and CNT-*g*-*sx*PS@Cu/Li (or bare Cu/Li) as the working electrodes. Notably, CNT-*g*-*sx*PS@Cu/Li (or bare Cu/Li) were fabricated by depositing 10 mAh cm^{-2} Li on CNT-*g*-*sx*PS@Cu (or bare Cu) substrates. Li|LFP full cells were assembled with CNT-*g*-*sx*PS@Cu/Li (or bare Cu/Li) anodes and $LiFePO_4$ cathodes (load-

ing = 2 mg cm^{-2}), and the electrolyte was 1 mol L^{-1} $LiPF_6$ in a mixture of ethylene carbonate/diethyl carbonate (1 ∶ 1 by volume). Li|NCM622 full cells were assembled with CNT-*g*-*sx*PS@Cu/Li anodes and $LiNi_{0.6}Co_{0.2}Mn_{0.2}O_2$ cathodes, and the electrolyte was 1.0 mol L^{-1} $LiPF_6$ in ethylene carbonate/diethyl carbonate/ethyl methyl carbonate (1 ∶ 1 ∶ 1 by volume). Unless otherwise specified, the loading of NCM622 cathode material is controlled at 1.5 mg cm^{-2}. The voltage windows of Li|LFP and Li|NCM622 full cells were set to 2.0-4.0 and 3.0-4.3 V, respectively. Electrochemical impedance spectra (EIS) were performed by applying alternating-current amplitude of 5 mV over the frequency range from 1 MHz to 0.1 Hz on an electrochemistry workstation.

3 Results and discussion

The synthetic route for CNT-*g*-*sx*PS is illustrated in Fig. 1b. Polystyrene (PS) brushes with carbon nanotube substrates (CNT-*g*-PS) were obtained by grafting PS side-chains from the surface-modified carbon nanotubes *via* the SI-ATRP strategy. SEM images indicate that as-obtained CNT-*g*-PS brushes possess well-defined 1D structure with increased diameters (Fig. 2a and b). According to FTIR spectra (Fig. S1), four characteristic peaks of benzene ring (1 486, 1 446, 748 and 694 cm^{-1}) and two methylene adsorption peaks (3 020 and 2 910 cm^{-1}) can be observed in CNT-*g*-PS in comparsion with Br-modified CNT (CNT-Br), further demonstrating the existence of PS[21]. The mass content of PS is calculated to be 20.5% (mass fraction) from the TGA curves of CNT-*g*-PS, CNT-Br and PS (Fig. S2). Cross-linked CNT-*g*-PS (CNT-*g*-*x*PS) were prepared *via* Friedel-Crafts reaction between phenyl rings in PS side-chains and carbon tetrachloride[19,22]. As shown in Fig. 2c, CNT-*g*-*x*PS display a similar interconnected 3D nanonetwork to CNT-*g*-PS, suggesting outstanding nanostructural inheritability. N_2 adsorption-desorption isotherm and DFT pore size distribution curve demonstrate a hierarchical porous structure of CNT-*g*-*x*PS (Fig. S3). An uptake at low relative pressures in CNT-*g*-*x*PS suggests the presence of micropores, which are derived from cross-linked PS side-chains. A hysteresis loop at medium relative pressures and a gradual increase of the adsorption amount at high relative pressures indicate the existence of meso- and macropores, respectively, which may be derived from the compact and loose covalent aggregation of CNT-*g*-*x*PS.

Vulcanization reaction was proceeded in the mixture of CNT-*g*-*x*PS and elemental sulfur with a two-step heating treatment process. As shown in Fig. 2d,

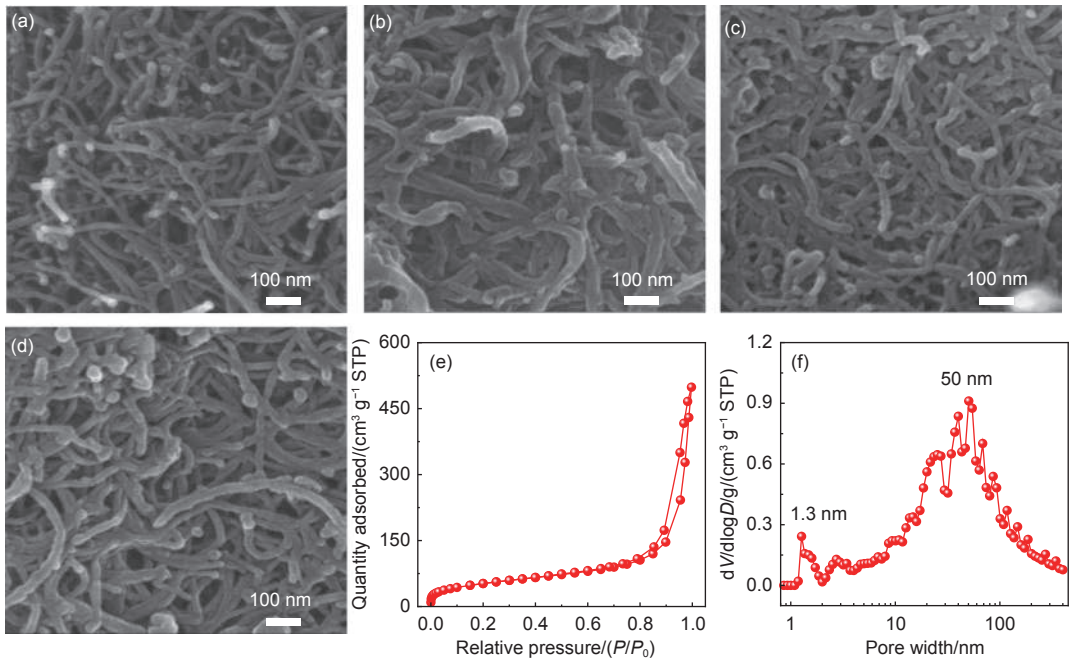

Fig. 2 SEM images of (a) CNT, (b) CNT-*g*-PS, (c) CNT-*g*-*x*PS and (d) CNT-*g*-*sx*PS. (e) N_2 adsorption-desorption isotherm and (f) pore size distribution curve of CNT-*g*-*sx*PS

the as-obtained CNT-*g*-*sx*PS still retain a 3D nanonetwork structure without any obvious sulfur aggregation. The mass contents of vulcanized hypercross-linked PS (*sx*PS) and carbon nanotube substrates are calculated to be 46.4% and 53.6% (mass fraction), respectively, from the TGA curves of CNT-Br (Fig. S2), CNT-*g*-*sx*PS, and *sx*PS (Fig. S4)[23]. The elemental mapping analysis further demonstrates the homogeneous distribution of sulfur element in CNT-*g*-*sx*PS (Fig. S5). As shown in Fig. S6, there is no sharp peaks identical to elemental sulfur in the XRD pattern of CNT-*g*-*sx*PS, demonstrating the chemical bonding of sulfur into CNT-*g*-*sx*PS skeletons during vulcanization. N_2 adsorption-desorption isotherm shows hierarchical micro-, meso- and macropores in CNT-*g*-*sx*PS with a S_{BET} of 178 $m^2\ g^{-1}$ (Fig. 2e). According to the DFT pore size distribution curve, the micropores in CNT-*g*-*sx*PS are centered at 1.3 nm while the meso/macropores range from 2 to 400 nm with a maximum at 50 nm (Fig. 2f). XPS measurements were carried out to further clarify the chemical states of sulfur. As shown in Fig. 3a, C—S (161.9 eV)

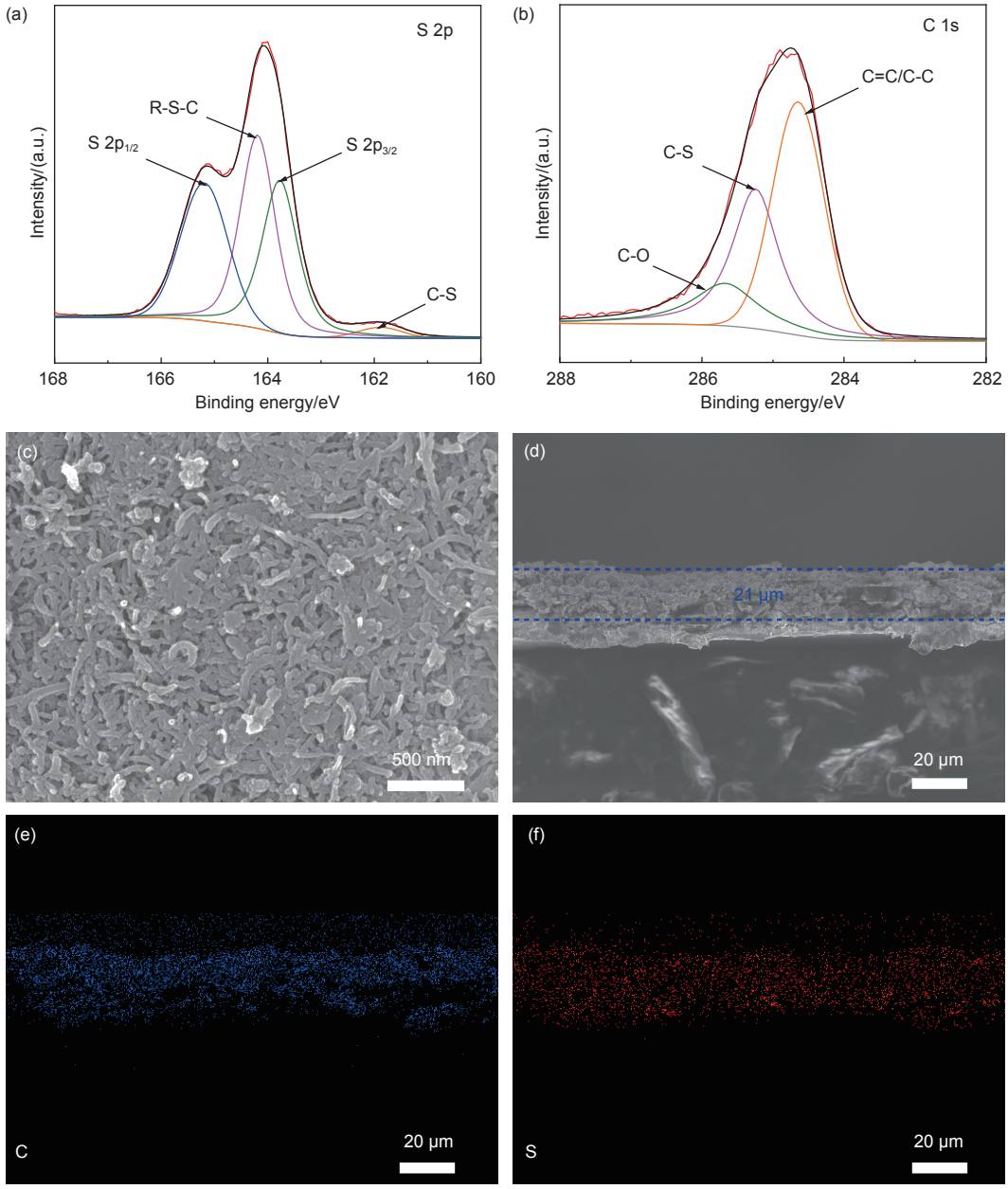

Fig. 3　(a) S 2p and (b) C 1s high-resolution XPS spectra of CNT-*g*-*sx*PS. (c) Top-view SEM image of CNT-*g*-*sx*PS@Cu. (d-f) Cross-section SEM image and corresponding elemental mapping images of CNT-*g*-*sx*PS@Cu

and R—S—C (164.2 eV) can be fitted in high-resolution S 2p spectrum, and the peaks at 163.8 and 165.2 eV are attributed to S—S bonds[24–26]. In high-resolution C 1s spectrum, the peak at 285.2 eV also confirms the presence of C—S bonds (Fig. 3b), revealing chemical bonds between sulfur and CNT-*g*-*sx*PS skeletons[27]. Benefiting from the good combination of lithiophilic sulfur groups with a hierarchical porous structure, CNT-*g*-*sx*PS would demonstrate great advantages to regulate Li nucleation and growth properties.

CNT-*g*-*sx*PS blade-coated on Cu foil (denoted as CNT-*g*-*sx*PS@Cu) were obtained to validate the feasibility of CNT-*g*-*sx*PS as 3D Li hosts. As shown in Fig. 3c, the top-view SEM image indicates CNT-*g*-*sx*PS are uniformly coated onto Cu foil. The cross-section SEM image and corresponding elemental mapping analysis display a 21 μm-thickness of CNT-*g*-*sx*PS with homogeneously distributed sulfur element (Fig. 3d-f). In order to clarify the effect of CNT-*g*-*sx*PS in regulating Li plating/stripping behavior, Li|Cu half-cells were assembled. The voltage-areal capacity curves are used to determine the Li deposition overpotential which can be divided to nucleation overpotential (μ_{nuc}) and mass transfer-controlled plateau potential (μ_{pla})[4]. As shown in Fig. S7, both μ_{nuc} and μ_{pla} of CNT-*g*-*sx*PS@Cu are lower than those of bare Cu, demonstrating that lithiophilic skeletons in CNT-*g*-*sx*PS can significantly reduce nucleation barrier and enhance Li transport kinetics[28].

After 10 mAh cm^{-2} Li was plated on CNT-*g*-*sx*PS@Cu (or bare Cu), as-obtained CNT-*g*-*sx*PS@Cu/Li anode demonstrates a smooth and compact surface in comparison with bare Cu/Li anode (Fig. S8). To further investigate the compositions and states of SEI in detail, XPS measurements were conducted on the surfaces of CNT-*g*-*sx*PS@Cu/Li and bare Cu/Li. As shown in Fig. 4a-c for bare Cu/Li, the signals of C=O, C—O, C—C/C=C, LiTFSI and SO_3^{2-} are derived from the electrolyte, while LiF (56.2 eV) and Li_2CO_3 (55.1 eV) peaks are attributed to classical SEI components[29–30]. In terms of CNT-*g*-*sx*PS@Cu/Li, the reduced peak intensities for electrolyte and the emergency of C-S signal (285.2 eV) suggest that CNT-*g*-*sx*PS participate in the construction of SEI and effectively alleviate the decomposition of electrolyte (Fig. 4d). Notably, the peaks at 162.3 eV in S 2p spectrum and the signal of 54.6 eV in Li 1s spectrum confirm Li_2S is included in SEI components (Fig. 4e and f)[28–29,31]. According to the above analysis, Li_2S-con-

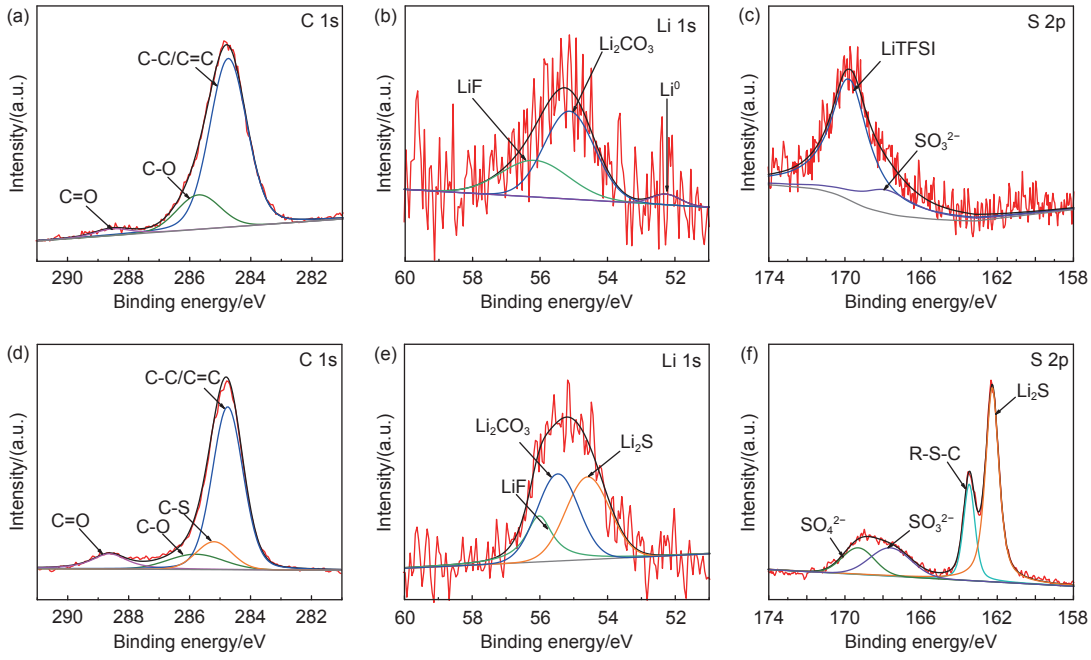

Fig. 4 (a) C 1s, (b) Li 1s and (c) S 2p high-resolution XPS spectra on the surface of bare Cu/Li. (d) C 1s, (e) Li 1s and (f) S 2p high-resolution XPS spectra on the surface of CNT-*g*-*sx*PS@Cu/Li

taining SEI is *in-situ* generated between Li and CNT-*g*-*sx*PS, which is beneficial for rapid Li flux and robust anode/electrolyte interface.

The Li|Cu half-cell displays a high average coulombic efficiency of 99.6% at 1 mA cm^{-2} and 1 mAh cm^{-2}, demonstrating the advantages of CNT-*g*-*sx*PS host in regulating Li nucleation and growth properties (Fig. S9). Symmetric Li|Li cells were fabricated to investigate the cycling stability of the CNT-*g*-*sx*PS@Cu/Li anodes. Nyquist plots of the cell with the CNT-*g*-*sx*PS@Cu/Li demonstrates enhanced Li ion transport kinetics in comparison with bare Cu/Li (Fig. 5a), which can be also reflected in the improved rate performance at all current densities of galvanostatic cycling test (Fig. 5b). The Li|Li symmetric cell with the CNT-*g*-*sx*PS@Cu/Li anode presents a critical current density of 14 mA cm^{-2}, which is higher than that of the cell with bare Cu/Li anode (11 mA cm^{-2}; Fig. S10). The cell with the CNT-*g*-*sx*PS@Cu/Li shows stable voltage profiles of more than 500 h with a small overpotential of 21 mV at 1 mA cm^{-2} and 1 mAh cm^{-2},which performs much better than the cell with bare Cu/Li (Fig. 5c). Their significant discrepancy in Li plating/stripping behaviors can be attrib-

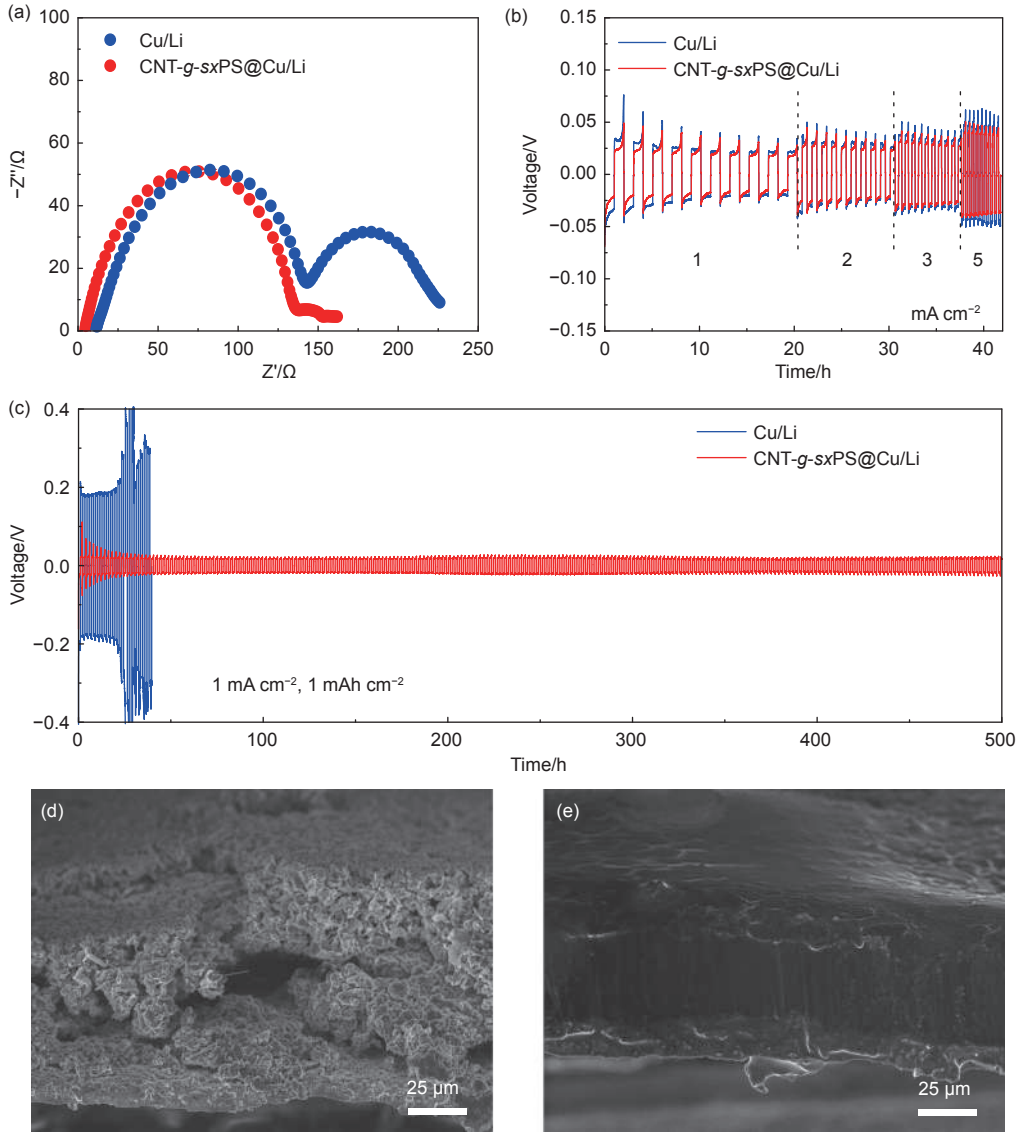

Fig. 5　(a) Nyquist plots of Li|Li symmetric cells with CNT-*g*-*sx*PS@Cu/Li and bare Cu/Li anodes. (b) Voltage profiles of symmetric Li|Li cells with CNT-*g*-*sx*PS@Cu/Li and bare Cu/Li anodes at various current densities with a fixed capacity of 1 mAh cm^{-2}. (c) Voltage profiles of Li|Li symmetric cells with CNT-*g*-*sx*PS@Cu/Li and bare Cu/Li anodes at 1 mA cm^{-2} and 1 mAh cm^{-2}. Cross-section SEM images of (d) bare Cu/Li and (e) CNT-*g*-*sx*PS@Cu/Li anodes after Li|Li symmetric cell tests for 50 cycles at 1 mA cm^{-2} and 1 mAh cm^{-2}

uted to the hierarchical porous structure and robust Li_2S-containing SEI. To the best of our knowledge, this performance compares favorably with those of many reported carbon-based Li hosts (Table S1). After cycling test, Li|Li symmetric cells were disassembled to further investigate the nanomorphologies of anodes. The top-view and cross-section SEM images show a highly porous structure with obvious dendrites in the cell with bare Cu/Li (Fig. S11a and Fig. 5d). As for the CNT-*g*-*sx*PS@Cu/Li, a flat and dense structure can be observed (Fig. S11b and Fig. 5e). These results demonstrate that the porous CNT-*g*-*sx*PS with uniformly distributed sulfur groups can effectively suppress Li dendrites and alleviate anode volume fluctuation.

The superiority of CNT-*g*-*sx*PS@Cu/Li anodes were further certified in full cell configurations. Nyquist plot of Li|LFP cell with CNT-*g*-*sx*PS@Cu/Li shows smaller semicircle at the high frequency region than the cell with bare Cu/Li (Fig. 6a), indicating the

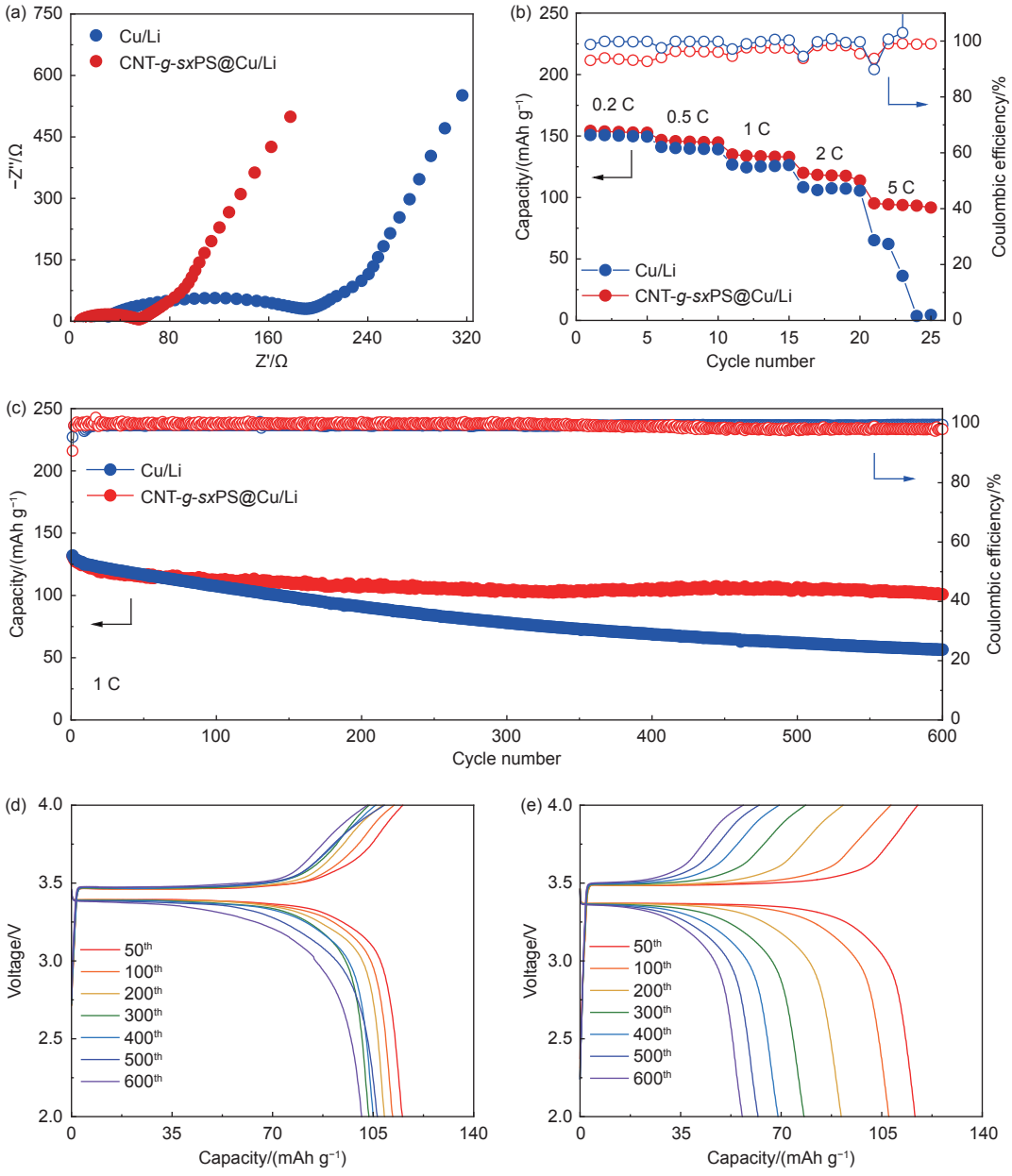

Fig. 6 (a) Nyquist plots of Li|LFP full cells with CNT-*g*-*sx*PS@Cu/Li and bare Cu/Li anodes. (b) Rate performance of Li|LFP full cells with CNT-*g*-*sx*PS@Cu/Li and bare Cu/Li anodes. (c) Cycling performance of Li|LFP full cells with CNT-*g*-*sx*PS@Cu/Li and bare Cu/Li anodes at 1 C. Galvanostatic charge-discharge profiles of Li|LFP cells with (d) CNT-*g*-*sx*PS@Cu/Li and (e) bare Cu/Li anodes

reduced interfacial impedance and enhanced Li ion transport kinetics. In terms of rate performance, the cell with CNT-*g*-*sx*PS@Cu/Li delivers average capacities of 153, 146 and 134 mAh g^{-1} under current densities of 0.2, 0.5 and 1 C, respectively. Even at a high current density of 5 C, a superior discharge capacity of 94 mAh g^{-1} can still be achieved, whereas severe capacity decay and even cell failure are observed in the cell with bare Cu/Li (Fig. 6b). The cell with CNT-*g*-*sx*PS@Cu/Li anode delivers a high discharge capacity of 101 mAh g^{-1} with a capacity retention of 77% after 600 cycles at 1 C (Fig. 6c). In sharp contrast, the cell with bare Cu/Li anode shows severe capacity decay with only 57 mAh g^{-1} after 600 cycles at 1 C, as evidenced by the voltage-capacity profiles in Fig. 6d, e. The remarkable performance difference can be further verified in full cell configuration evaluation with NCM622 cathodes. The cell with CNT-*g*-*sx*PS@Cu/Li anode displays excellent rate performance, with average capacities of 166, 159 and 152 mAh g^{-1} under current densities of 0.2, 0.5 and 1 C, respectively (Fig. S12a). Even at a high current density of 5 C, the cell with CNT-*g*-*sx*PS@Cu/Li anode still delivers a high average capacity of 127 mAh g^{-1}. As the current density returns back to 0.2 C, the cell with CNT-*g*-*sx*PS@Cu/Li anode resumes an average capacity of 164 mAh g^{-1}. In sharp contrast, the cell with bare Cu/Li anode shows significantly inferior rate performance with rapidly attenuated average capacities at 1 C (108 mAh g^{-1}) and 2 C (71 mAh g^{-1}), and comes into failure at 5 C. Even when paired with high-loading NCM622 cathodes (21.6 mg cm^{-2}, ~ 4 mAh cm^{-2}), the full cell with CNT-*g*-*sx*PS@Cu/Li also delivers a high initial discharge capacity of 169 mAh g^{-1} at 0.1 C and retains an excellent capacity retention ratio of 98% for 30 cycles (Fig. S12b).

4 Conclusion

In summary, we have successfully developed a novel class of vulcanized cross-linked polystyrene grafted on carbon nanotubes (CNT-*g*-*sx*PS) as advanced Li hosts. On the one hand, the hierarchical macro-, meso- and microporous structure of CNT-*g*-*sx*PS can accelerate Li ion transport, alleviate volume changes of Li anode and reduce local current density, which is conductive to rapid and homogeneous Li plating/stripping. On the other hand, uniformly distributed sulfur groups in porous skeleton can react with Li to *in-situ* generate a Li_2S-containing SEI layer, contributing to a robust anode/electrolyte interface. Moreover, carbon nanotube substrates enable rapid transmission of electrons. As a result, Li|Li symmetric cell with CNT-*g*-*sx*PS@Cu/Li anode exhibits stable cycling performance of more than 500 h at a current density of 1 mA cm^{-2} and 1 mAh cm^{-2}. When paired with LFP cathode, the full cell with CNT-*g*-*sx*PS@Cu/Li delivers a high discharge capacity of 101 mAh g^{-1} with a capacity retention ratio of 77% after 600 cycles at 1 C. Our work demonstrates a unique molecular topological engineering design to simultaneously construct high-lithiophilicity host as well as robust SEI layer, which is expected to shed light on the construction of multifunctional Li hosts for dendrite-free and interface-stable LMBs.

Acknowledgements

This work was supported by National Key Research and Development Program of China (2021YFF0500600) and National Natural Science Foundation of China (51925308).

References

[1] Tarascon J, Armand M. Issues and challenges facing rechargeable lithium batteries[J]. Nature, 2001, 414(6861): 359-367.

[2] Zhang X, Yang Y, Zhou Z. Towards practical lithium-metal anodes[J]. Chemical Society Review, 2020, 49(10): 3040-3071.

[3] Li S, Huang J, Cui Y, et al. A robust all-organic protective layer towards ultrahigh-rate and large-capacity Li metal anodes[J]. Nature Nanotechnology, 2022, 17(6): 613-621.

[4] Chen X, Zhao B, Yan C, et al. Review on Li deposition in working batteries: from nucleation to early growth[J]. Advanced Materials, 2021, 33(8): e2004128.

[5] Li C, Liu S, Shi C, et al. Two-dimensional molecular brush-functionalized porous bilayer composite separators toward ultrastable high-current density lithium metal anodes[J]. Nature Communications, 2019, 10(1): 1363.

[6] He X, Bresser D, Passerini S, et al. The passivity of lithium

electrodes in liquid electrolytes for secondary batteries[J]. Nature Reviews Materials, 2021, 6(11): 1036-1052.

[7] Liu Q, Liu R, Cui Y, et al. Dendrite-free and long-cycling lithium metal battery enabled by ultrathin, 2D shield-defensive, and single lithium-ion conducting polymeric membrane[J]. Advanced Materials, 2022, 34(33): e2108437.

[8] Li S, Zhang L, Liu T, et al. A dendrite-free lithium-metal anode enabled by designed ultrathin MgF_2 nanosheets encapsulated inside nitrogen-doped graphene-like hollow nanospheres[J]. Advanced Materials, 2022, 34(24): e2201801.

[9] Fang Y, Zhang S, Wu Z, et al. A highly stable lithium metal anode enabled by Ag nanoparticle-embedded nitrogen-doped carbon macroporous fibers[J]. Science Advances, 2021, 7(21): eabg3626.

[10] Mei Y, Zhou J, Hao Y, et al. High-lithiophilicity host with micro/nanostructured active sites based on wenzel wetting model for dendrite - free lithium metal anodes[J]. Advanced Functional Materials, 2021, 31(50): 2106676.

[11] Lu Z, Liu S, Li C, et al. 3D porous carbon networks with highly dispersed SiO_x by molecular-scale engineering toward stable lithium metal anodes[J]. Chemical Communication, 2019, 55(43): 6034-6037.

[12] Chen C, Guan J, Li N, et al. Lotus-root-like carbon fibers embedded with Ni-Co nanoparticles for dendrite-free lithium metal anodes[J]. Advanced Materials, 2021, 33(24): e2100608.

[13] Huang G, Han J, Zhang F, et al. Lithiophilic 3D nanoporous nitrogen-doped graphene for dendrite-free and ultrahigh-rate lithium-metal anodes[J]. Advanced Materials, 2019, 31(2): e1805334.

[14] Wang J, Li L, Hu H, et al. Toward dendrite-free metallic lithium anodes: from structural design to optimal electrochemical diffusion kinetics[J]. ACS Nano, 2022, 16(11): 17729-17760.

[15] Fan L, Zhuang H, Zhang W, et al. Stable lithium electrodeposition at ultra-high current densities enabled by 3D PMF/Li composite Anode[J]. Advanced Energy Materials, 2018, 8(15): 1703360.

[16] Hu Z, Deng W, He B, et al. Self-adaptive 3D skeleton with charge dissipation capability for practical Li metal pouch cells[J]. Nano Energy, 2022, 93(106805).

[17] Ma Y, Wei L, He Y, et al. A "blockchain" synergy in conductive polymer-filled metal-organic frameworks for dendrite-free Li plating/stripping with high coulombic efficiency[J]. Angewandte Chemie International Edition, 2022, 61(12): e202116291.

[18] Yang Z, Liu W, Chen Q, et al. Ultrasmooth and dense lithium deposition toward high-performance lithium-metal batteries[J]. Advanced Materials, 2023: e2210130.

[19] Liang Y, Chen L, Zhuang D, et al. Fabrication and nanostructure control of super-hierarchical carbon materials from heterogeneous bottlebrushes[J]. Chemical Science, 2017, 8(3): 2101-2106.

[20] Adams B, Zheng J, Ren X, et al. Accurate determination of coulombic efficiency for lithium metal anodes and lithium metal batteries[J]. Advanced Energy Materials, 2018, 8(7): 1702097.

[21] Chen G, Liu S, Chen S, et al. FTIR spectra, thermal properties, and dispersibility of a polystyrene/montmorillonite nanocomposite[J]. Macromolecular Chemistry and Physics, 2001, 202(7): 1189-1193.

[22] Li Z, Wu D, Liang Y, et al. Synthesis of well-defined microporous carbons by molecular-scale templating with polyhedral oligomeric silsesquioxane moieties[J]. Journal of the American Chemical Society, 2014, 136(13): 4805-4808.

[23] Wu J, Huang J, Cui Y, et al. Rough endoplasmic reticulum inspired polystyrene-brush-based superhigh sulfur content cathodes enable lithium-sulfur cells with high mass and capacity loading[J]. Advanced Materials, 2023: e2211471.

[24] Wu P, Sun M, Yu Y, et al. Physical and chemical dual-confinement of polysulfides within hierarchically meso-microporous nitrogen-doped carbon nanocages for advanced Li –S batteries[J]. RSC Advances, 2017, 7(68): 42627-42633.

[25] Chua C & Pumera M. Monothiolation and reduction of graphene oxide via one-pot synthesis: Hybrid catalyst for oxygen reduction[J]. ACS Nano, 2015, 9(4): 4193-4199.

[26] Hu G, Sun Z, Shi C, et al. A sulfur-rich copolymer@CNT hybrid cathode with dual-confinement of polysulfides for high-performance lithium-sulfur batteries[J]. Advanced Materials, 2017, 29(11): 1603835.

[27] Munir A, Haq T, Qurashi A, et al. Ultrasmall Ni/NiO nanoclusters on thiol-functionalized and -exfoliated graphene oxide nanosheets for durable oxygen evolution reaction[J]. ACS Applied Energy Materials, 2018, 2(1): 363-371.

[28] Zhang T, Li J, Li X, et al. A silica-reinforced composite electrolyte with greatly enhanced interfacial lithium-ion transfer kinetics for high-performance lithium metal batteries[J]. Advanced Materials, 2022, 34(41): 2205575.

[29] Liang J, Li X, Zhao Y, et al. In situ Li_3PS_4 solid-state electrolyte protection layers for superior long-life and high-rate lithium-metal anodes[J]. Advanced Materials, 2018, 30(45): 1804684.

[30] Wang W, Yang Z, Zhang Y, et al. Highly stable lithium metal anode enabled by lithiophilic and spatial-confined spherical-covalent organic framework[J]. Energy Storage Materials, 2022, 46(374-383).

[31] Tian M, Ben L, Yu H, et al. Designer cathode additive for stableinterphases on high-energy anodes[J]. Journal of the American Chemical Society, 2022, 144(33): 15100-15110.